October, 1993

QCD CORRECTIONS TO HIGGS BOSON PRODUCTION: NON-LEADING TERMS IN THE HEAVY QUARK LIMIT

S. Dawson and R. Kauffman*

Physics Department
Brookhaven National Laboratory, Upton, NY 11973

We compute analytic results for the QCD corrections to Higgs boson production via gluon fusion in hadronic collisions in the limit in which the top quark is much heavier than the Higgs boson. The first non-leading corrections of $\mathcal{O}(\alpha_s^3 M_H^2/m_t^2)$ are given and numerical results presented for both LHC and SSC energies. We confirm earlier numerical results showing that the dominant corrections have the same mass dependence as the Born cross section.

* This manuscript has been authored under contract number DE-AC02-76-CH-00016 with the U.S. Department of Energy. Accordingly, the U.S. Government retains a non-exclusive, royalty-free license to publish or reproduce the published form of this contribution, or allow others to do so, for U.S. Government purposes.

1. INTRODUCTION

One of the prime motivations for the construction of high energy hadron colliders is to unravel the mechanism of electroweak symmetry breaking. In the standard model of electroweak interactions there exists a physical scalar boson, called the Higgs boson, whose interactions generate the non-zero masses of the W and Z gauge bosons.[1] The couplings of the Higgs boson are completely specified in the standard model; the only unknown parameter is its mass. For a given mass, therefore, it is possible to predict the properties and production mechanisms of the standard model Higgs boson unambiguously. In this paper, we discuss the two-loop QCD radiative corrections of $\mathcal{O}(\alpha_s^3)$ to the production of the Higgs boson in hadronic interactions.

A particularly interesting mass region in which to search for the Higgs boson is the intermediate mass region, $80 \lesssim M_{\rm H} \lesssim 150$ GeV. The dominant decay mode for the intermediate mass Higgs boson is $H \to b\bar{b}$. However, the formidable QCD background to this decay will probably necessitate using rare decay modes such as $H \to \gamma\gamma$ to search for the intermediate mass Higgs boson. Since the number of events remaining after cuts to remove backgrounds is small, it is vital to understand the effects of radiative corrections in this region in order to determine the viability of the signal.

In the intermediate mass region, the primary production mechanism is gluon fusion through a top quark loop as shown in Fig. 1. For a heavy top quark, $m_t \gtrsim 150$ GeV, and an intermediate-mass Higgs boson it makes sense to expand the results in powers of $r \equiv M_{\rm H}^2/m_t^2$. The zeroth-order result in this expansion, *i.e.*, the $m_t \to \infty$ limit, is remarkably accurate, giving the amplitude in Fig. 1 to better than 10% even up to $r = 1$. However, there is no guarantee that the radiative corrections will have as little dependence on r.

The leading corrections for $m_t \to \infty$ have been computed previously and found to increase the cross section by about a factor of two. Thus, it is critical to determine

the m_t dependence of the radiatively-corrected cross section. In this paper we take the natural first step : we compute the first non-leading corrections of $\mathcal{O}(\alpha_s^3 r)$ to Higgs boson production in hadronic collisions. In such a limit, the computation of the two loop QCD radiative corrections becomes greatly simplified and it is possible to obtain analytic results.[2,3] Our analytical results (for the region over which they are valid) confirm the numerical results of Ref. 3, valid for arbitrary M_H/m_t.

If the top quark is very heavy it will show up indirectly via its contribution to radiative corrections to various quantities such as the W and Z masses. Indeed, a global fit to existing data from electroweak processes requires $m_t \lesssim 180$ GeV for the consistency of the standard model.[4] For the intermediate mass Higgs boson, say $M_H \sim 100$ GeV, the $m_t \gg M_H$ limit may be a reasonable approximation. For a heavy Higgs boson, such as $M_H \sim 1$ TeV, the $m_t \to \infty$ limit clearly is not valid. In this case, our results can be used to gauge the sensitivity of the Higgs boson production rate to new physics, since any new heavy quarks will contribute to Higgs production from gluon fusion. For example, a doublet of heavy quarks which is degenerate in mass would not contribute to the ρ parameter, but would contribute to the gluon fusion production of a Higgs boson.

The organization of the paper is as follows. In Section 2, we review previous results and describe how the low energy theorems are used to obtain the $\mathcal{O}(\alpha_s^3)$ corrections to the process $gg \to H$ in the limit in which $m_t \to \infty$. Section 3 contains a description of the calculational techniques required to compute the two loop integrals occuring in the evaluation of the virtual diagrams for gluon fusion when the non-leading terms in M_H/m_t are retained. In Section 4 we present our analytical results: partonic cross sections for gg, $q\bar{q}$ and $qg \to H + X$ to $\mathcal{O}(\alpha_s^3 r)$. Section 5 contains numerical results for Higgs boson production in pp interactions at $\sqrt{S} = 15$ TeV and $\sqrt{S} = 40$ TeV. Finally, we present our conclusions in Section 6. The appendices contain details pertaining to the evaluation of the two-loop integrals.

2. PREVIOUS RESULTS

The lowest order amplitude for the gluon fusion of a Higgs boson arises at one loop from the triangle diagram of Fig.1. The amplitude is sensitive to all of the quarks but since the coupling of quarks to the Higgs boson is proportional to their mass the contribution from light quarks is suppressed. Assuming there are no heavier quarks, the contribution from the top quark is dominant over the range in $M_{\rm H}$ currently allowed by experiment ($M_{\rm H} > 60$ GeV[5]). The contribution to the amplitude from a single heavy quark with mass m_q has been available in the literature for some time,[6]

$$\mathcal{A}_0^{\mu\nu}\left(g_{\rm A}^{\mu}(k_1)g_{\rm B}^{\nu}(k_2) \to H\right) = -\frac{\alpha_s}{2\pi v}\delta_{\rm AB}(k_1\cdot k_2 g^{\mu\nu} - k_1^{\nu}k_2^{\mu})\tau_q\left[1+(1-\tau_q)f(\tau_q)\right] \quad , \tag{2.1}$$

where $v^2 = (\sqrt{2}G_F)^{-1} = (246\ \text{GeV})^2$, $\tau_q \equiv 4m_q^2/M_{\rm H}^2$, and

$$f(\tau_q) = \begin{cases} \left[\sin^{-1}\left(\sqrt{\frac{1}{\tau_q}}\right)\right]^2, & \text{if } \tau_q \geq 1, \\ -\frac{1}{4}\left[\log\left(\frac{\eta_+}{\eta_-}\right) - i\pi\right]^2, & \text{if } \tau_q < 1, \end{cases} \tag{2.2}$$

with

$$\eta_{\pm} \equiv 1 \pm \sqrt{1-\tau_q} \quad . \tag{2.3}$$

Taking the limit $r = M_{\rm H}^2/m_t^2 \ll 1$,

$$\mathcal{A}_0^{\mu\nu} \to -\frac{\alpha_s}{3\pi v}\mathcal{N}\delta_{\rm AB}\left[1+\frac{7r}{120}(1+\epsilon)\right](k_1\cdot k_2 g^{\mu\nu} - k_1^{\nu}k_2^{\mu}) \quad . \tag{2.4}$$

Neglecting contributions from light quarks, this gives the spin and color averaged cross section,

$$\begin{aligned}\sigma_0(gg \to H) &\to \frac{\alpha_s^2}{\pi}\frac{M_{\rm H}^2}{576v^2}\mathcal{N}^2\frac{1}{1-\epsilon}\left[1+\frac{7r}{60}(1+\epsilon)\right]\delta(s-M_{\rm H}^2) \\ &\equiv \sigma_0^{\epsilon}M_{\rm H}^2\delta(s-M_{\rm H}^2) \quad ,\end{aligned} \tag{2.5}$$

with

$$\mathcal{N} = \left[\left(\frac{4\pi}{m_t^2} \right)^{\epsilon} \Gamma(1+\epsilon) \right] \quad ,$$

where we have computed the amplitude and cross section in $n = 4 - 2\epsilon$ dimensions for later use.

When the momentum transfer to the Higgs boson is small, or equivalently in the limit $m_t \gg M_{\rm H}$, the cross section to $\mathcal{O}(\alpha_s^3)$ for $gg \to H$ can be obtained from the effective Lagrangian,[7]

$$\mathcal{L}_{\rm eff} = -\frac{1}{4}\left[1 - \frac{2H}{v} \frac{\beta_F}{g(1+\delta)} \right] G^{\mu\nu}_{\rm A} G^{\rm A}_{\mu\nu} \quad , \tag{2.6}$$

where $G^A_{\mu\nu}$ is the gluon field strength tensor and β_F is the contribution of the top quark to the QCD beta function:

$$\frac{\beta_F}{g} = \frac{\alpha_s}{6\pi}\left\{ 1 + \frac{\alpha_s}{\pi}\frac{19}{4} \right\} \quad . \tag{2.7}$$

The $(1+\delta)$ term arises from a subtlety in the use of the low-energy theorem.[8] Since the Higgs coupling to heavy fermions is $m_t(1 + H/v)\bar{t}t$, the counterterm for the Higgs Yukawa coupling is fixed in terms of the renormalization of the fermion mass and wave function. In the $\overline{\rm MS}$ scheme, $\delta = 2\alpha_s/\pi$.[8,9] In the limit $m_t \gg M_{\rm H}$, the effective Lagrangian of Eq. (2.6) can be used to obtain the gluonic radiative corrections of $\mathcal{O}(\alpha_s^3)$ from a one-loop calculation.[2,3] This serves as a valuable check of the complete two-loop calculation. An effective Lagrangian approach can also be used to obtain the $\mathcal{O}(\alpha_s^3)$ radiative corrections to the gluon fusion of a pseudoscalar, $gg \to A^0$.[10]

We proceed to calculate the terms of $\mathcal{O}(\alpha_s^3 r)$. Unfortunately, the $\mathcal{O}(r)$ corrections to the effective Lagrangian are not known and to obtain them would require a two-loop calculation. It is simpler to perform the direct calculation; the necessary techniques are discussed in the next section.

3. CALCULATIONAL TECHNIQUES

The evaluation of the two-loop diagrams arising in the virtual corrections to $gg \to H$ is an extension of the techniques used in the case of $H \to \gamma\gamma$.[11] The basic strategy is to expand the loop integrals in powers of the external momenta over m_t at every stage.[12] This technique has been successfully used to compute the 2–loop contribution to the ρ parameter from a heavy top quark.[13] The complete set of two-loop diagrams is shown in Fig. 2. Each graph gives a result of the form

$$\mathcal{A}_i^{\mu\nu} = C\,(a_i g^{\mu\nu} k_1 \cdot k_2 + b_i k_1^\nu k_2^\mu + c_i k_1^\mu k_2^\nu) \quad , \tag{3.1}$$

where the incoming gluons have momenta, polarization indices and colors as in Eq. (2.1)and

$$C \equiv -\mathcal{N}^{-2}\delta_{AB}\frac{\alpha_s^2}{2\pi^2 v} \quad . \tag{3.2}$$

Gauge invariance requires that

$$\sum_i a_i = -\sum_i b_i, \tag{3.3}$$

where the sum runs over all the diagrams. (The c_i terms do not contribute for on-shell gluons.) In order to reduce the number of tensor structures and deal with scalar quantities only, we compute three contractions of each diagram : $\mathcal{A}_i^{\mu\nu} g_{\mu\nu}$, $\mathcal{A}_i^{\mu\nu} k_{1\mu} k_{2\nu}$ and $\mathcal{A}_i^{\mu\nu} k_{1\nu} k_{2\mu}$. From the contracted amplitudes the values of a_i and b_i can easily be found

$$\begin{aligned} a_i &= \frac{\mathcal{A}_i^{\mu\nu}}{C(n-2)(k_1\cdot k_2)^2}\Big\{k_1\cdot k_2 g_{\mu\nu} - k_{1\nu}k_{2\mu} - k_{1\mu}k_{2\nu}\Big\}, \\ b_i &= \frac{\mathcal{A}_i^{\mu\nu}}{C(n-2)(k_1\cdot k_2)^2}\Big\{(n-1)k_{1\mu}k_{2\nu} - k_1\cdot k_2 g_{\mu\nu} + k_{1\nu}k_{2\mu}\Big\}. \end{aligned} \tag{3.4}$$

The various two-loop diagrams have either one, two or three gluon propagators. Diagrams with one gluon propagator (these are the ones previously calculated in Ref.

11) can be written such that the gluon propagator contains no external momenta. For those diagrams with more than one gluon propagator we Feynman parametrize to combine the massless gluon propagators (top quark propagators are left alone); the loop momenta are then shifted to move the external momenta into the top-quark propagators. The gluon propagators for diagrams V-VIII become

$$\begin{aligned}
\text{V–VI}: &\ \frac{1}{q^2(q-k_1)^2} \to \frac{1}{(q'^2)^2} \quad \text{where } q' = q - xk_1 \quad , \\
\text{VII}: &\ \frac{1}{(q+k_1)^2(q-k_2)^2} \to \frac{1}{(q'^2 + x(1-x)M_{\rm H}^2)^2} \\
&\qquad \text{where } q' = q + xk_1 - (1-x)k_2, \\
\text{VIII}: &\ \frac{1}{q^2(q+k_1)^2(q-k_2)^2} \to \frac{1}{(q'^2 + xyM_{\rm H}^2)^3} \quad \text{where } q' = q + xk_1 - yk_2 \quad ,
\end{aligned} \tag{3.5}$$

where the integrals over the Feynman parameters x and y are implicit. For diagrams V and VI all the external momentum can be shifted into the heavy-quark propagators. For diagrams VII and VIII products of $k_1 \cdot k_2 = M_{\rm H}^2/2$ and Feynman parameters remain in the denominators.

The denominators arising from the heavy-quark propagators in Fig. 2 can be expanded in powers of the external momentum, e.g.,

$$\frac{1}{(q-k_1)^2 - m_t^2} = \frac{1}{q - m_t^2}\left(1 + \frac{2q \cdot k_1}{q - m_t^2} + ...\right) \quad . \tag{3.6}$$

To obtain the terms of $\mathcal{O}(M_{\rm H}^2/m_t^2)$ each denominator must be expanded up to terms containing two powers each of k_1 and k_2 (in diagram VIII the denominators must be expanded to one further power because the momentum integrals bring in an inverse power of $M_{\rm H}^2$). The Feynman integrals for diagrams V and VI can be performed at this stage since the expansion brings the Feynman parameters into the numerator. The Feynman integrals for VII and VIII must be performed after the momentum integration but they involve only polynomials and logarithms and are easily done.

After contracting the amplitudes from the graphs of Fig. 2 as in Eq. (3.4) and expanding the denominators all the contributions have the form

$$\int \frac{d^n p}{(2\pi)^n} \int \frac{d^n q}{(2\pi)^n} \frac{(\text{powers of } p\cdot k_i, q\cdot k_i) \times (\text{powers of } p^2,\ q^2,\ p\cdot q)}{[(p+q)^2 - m^2]^j (p^2 - m_t^2)^k (q^2 - m_t^2)^l} \quad , \tag{3.7}$$

where m^2 can be zero or a product of Feynman parameters times $M_{\rm H}^2$. Using symmetry arguments the powers of $p\cdot k_i$ and $q\cdot k_i$ in the numerators can be written in terms of powers of p^2, q^2, and $p\cdot q$ times powers of $k_1\cdot k_2 = M_{\rm H}^2/2$. The integrals can then be reduced to the symmetric form [14]

$$\int \frac{d^n p}{(2\pi)^n} \int \frac{d^n q}{(2\pi)^n} \frac{1}{[(p+q)^2 - m^2]^j (p^2 - m_t^2)^k (q^2 - m_t^2)^l} \quad . \tag{3.8}$$

These integrals are well known in the literature and are discussed in Appendix A. The techniques necessary to symmetrize the numerators are discussed in Appendix B.

4. RESULTS

To compute the radiative corrections for the inclusive production of the Higgs boson from gluon fusion, we need both the real contribution from $gg \to gH$ and the virtual corrections to $gg \to H$. We will also need the contributions for $qg \to qgH$ and $q\bar{q} \to gH$.

(a) Virtual Corrections to $gg \to H$

The results of the two-loop diagrams contributing to $gg \to H$ are detailed in Appendix C. The sum of the two-loop amplitudes can be written in terms of the Born amplitude from Eq. (2.4), (neglecting the irrelevant imaginary part)

$$Re(\mathcal{A}_{\rm v}^{\mu\nu}) = \frac{\alpha_s}{2\pi} \mathcal{A}_0^{\mu\nu} \mathcal{N} \left[C_{\rm A} \left(-\frac{r^{-\epsilon}}{\epsilon^2} + \frac{5}{2} + \frac{2\pi^2}{3} - \frac{19r}{180} \right) - \frac{3C_{\rm F}}{2} \left(3 + \frac{7r}{60\epsilon} - \frac{13r}{1080} \right) \right] + \mathcal{O}(r^2) \quad . \tag{4.1}$$

The color factors for SU(3) are given by $C_{\rm A} = 3$ and $C_{\rm F} = 4/3$. The term proportional to $C_{\rm F}$ contributes to $H \to \gamma\gamma$ and was computed in Refs. 11, 15.

It is natural to group the mass counterterms on the fermion propagator and those at the $Ht\bar{t}$ vertex with the virtual corrections. The inclusion of the mass counterterms (which have no C_A component) renders the contribution proportional to C_F finite. We use the on-mass shell renormalization scheme in which the physical mass is defined to be the pole in the propagator. The renormalized fermion propagator is then:

$$\frac{i}{\not p - m_t}\left\{1 + \frac{\Sigma_R(p)}{\not p - m_t} + \ldots\right\} \tag{4.2}$$

where ‡1

$$\Sigma_R(p) = \Sigma(p) - \delta m_t - Z_2(\not p - m_t) \tag{4.3}$$

and

$$\frac{\delta m_t}{m_t} = \mathcal{N} C_F \frac{\alpha_s}{\pi}\left(\frac{3}{4\epsilon} + 1\right) \quad . \tag{4.4}$$

The sum of the mass counterterms is

$$\mathcal{A}^{\mu\nu}_{\delta m} = \mathcal{N}\frac{\alpha_s}{2\pi}\mathcal{A}_0^{\mu\nu} 3C_F\left(1 + \frac{7r}{120\epsilon} + \frac{49r}{360}\right) + \mathcal{O}(r^2) \quad . \tag{4.5}$$

Our result for the virtual amplitude plus mass counterterms, is then ($r \equiv M_H^2/m_t^2$):

$$Re(\mathcal{A}_v) = \frac{\alpha_s}{2\pi}\mathcal{A}_0\mathcal{N}\left[C_A\left(-\frac{r^{-\epsilon}}{\epsilon^2} + \frac{5}{2} + \frac{2\pi^2}{3} - \frac{19r}{180}\right) - \frac{3C_F}{2}\left(1 - \frac{307r}{1080}\right)\right] + \mathcal{O}(r^2) \tag{4.6}$$

which gives the contribution to the spin and color averaged cross section:

$$\begin{aligned}\sigma_{virt} =& \sigma_0^e \frac{\alpha_s}{\pi}\mathcal{N}\left\{C_A\left(-\frac{r^{-\epsilon}}{\epsilon^2} + \frac{5}{2} + \frac{2\pi^2}{3} - \frac{19r}{180}\right)\right. \\ &\left. - \frac{3C_F}{2}\left(1 - \frac{307r}{1080}\right)\right\}\delta(1-z) + \mathcal{O}(r^2) \quad ,\end{aligned} \tag{4.7}$$

where $z = M_H^2/s$ and σ_0^e is defined in Eq. (2.5) and contains the overall factor $[1 + 7r(1+\epsilon)/60]$.

---

‡1 The various factors of Z_2 on the fermion propagators and at the $H\bar{t}t$ vertex and the factors of Z_1 at the $g\bar{t}t$ vertices combine to give the charge renormalization counterterm given in Section 4c.

There are various checks we can perform on the contributions to Eq. (4.1). The diagrams VII and VIII have imaginary parts and terms proportional to $\log r$ and $\log^2 r$. The imaginary parts can be obtained via the Cutkosky rules and the $\log r$ terms can be related to them since they both arise from terms containing $\log(-r)$. The $1/\epsilon$ terms coming from diagrams VI and VIII are purely infrared and can computed by appropriately contracting the legs of the $ggqH$ box diagram. These various checks are described in Appendix D.

(b)Real Diagrams for $gg \to gH$

The matrix element squared for the process $gg \to gH$ can be found from the diagrams of Fig. 3.[16] The result, with the appropriate spin and color sums and averages, is

$$|\overline{\mathcal{A}}(gg \to gH)|^2 = 8\sigma_0^\epsilon C_A \alpha_s \left\{ \frac{s^4 + t^4 + u^4 + M_H^8}{stu} - \frac{rM_H^2}{10} \right\} + \mathcal{O}(r^2) \quad . \tag{4.8}$$

To make clear the structure of this result we write it terms of the $r = 0$ result from Ref. 2:

$$|\overline{\mathcal{A}}|^2 = \frac{\sigma_0^\epsilon}{\sigma_0^\epsilon(r=0)} |\overline{\mathcal{A}}(r=0)|^2 - \frac{8}{10}\sigma_0^\epsilon C_A \alpha_s r M_H^2 + \mathcal{O}(r^2) \quad . \tag{4.9}$$

We see that the bulk of the terms, and all those which yield infinities, have the same structure as the $r = 0$ result and are scaled by the m_t dependence of the Born cross section. Clearly, the soft and collinear singularities will factor as they must. The form of the extra $\mathcal{O}(r)$ term in Eq. (4.9) is determined by Bose symmetry: M_H^2 is the only term symmetric in s, t and u with the proper dimension. No terms which grow with s and would spoil the expansion are allowed.

Integrating over the phase space of the final state gluon, we find the contribution

to the cross section:

$$\sigma_{\rm real} = \sigma_0^\epsilon \frac{C_A \alpha_s}{\pi} \mathcal{N} r^{-\epsilon} \left\{ \left(\frac{1}{\epsilon^2} - \frac{\pi^2}{3} \right) \delta(1-z) - \frac{1}{\epsilon} z^{1+\epsilon} \tilde{P}_{gg}(z) \right.$$
$$+ 2 \left[\frac{\log(1-z)}{1-z} \right]_+ [1 + (1-z)^4 + z^4] - \frac{11}{6}(1-z)^3 \qquad (4.10)$$
$$\left. - \frac{rz(1-z)}{20} \right\} + O(r^2) \quad ,$$

where

$$\tilde{P}_{gg}(z) = 2 \left\{ \left(\frac{z}{1-z} \right)_+ + \frac{1-z}{z} + z(1-z) \right\} \quad . \qquad (4.11)$$

The plus distribution functions are defined,

$$\int \frac{f(x)}{(1-x)_+} \equiv \int \frac{f(x) - f(1)}{1-x} \quad . \qquad (4.12)$$

(c) Counterterms for $gg \to HX$

In addition to the mass counterterms included in the virtual diagrams, there are also counterterms due to the gluon wavefunction and charge renormalization.

For the charge renormalization, we use a modification of the $\overline{MS}$ scheme in which the top quark decouples as its mass goes to infinity.[17] In this scheme, the renormalized coupling is related to the bare coupling by,

$$\alpha_s^R = \alpha_s^0 \left\{ 1 - \frac{\alpha_s b_0}{\epsilon} \mathcal{N} \left(\frac{m_t^2}{\mu^2} \right)^\epsilon + \frac{\alpha_s}{6\pi\epsilon} \mathcal{N} \right\}$$
$$\equiv \left(1 + 2\delta Z_g \right) \alpha_s^0 \qquad (4.13)$$

where b_0 is the QCD β function:

$$b_0 = \frac{1}{4\pi} \left(\frac{11 C_A}{3} - \frac{2}{3} n_{lf} \right) \quad . \qquad (4.14)$$

The charge renormalization then gives a contribution to the cross section,

$$\sigma_{\rm ch} = 4\delta Z_g \sigma_0^\epsilon \delta(1-z) \quad . \qquad (4.15)$$

There is also a counterterm due to the wavefunction renormalization on the external

gluon legs:

$$\sigma_{\rm wf} = 4\delta Z_{\rm wf}\sigma_0^\epsilon\delta(1-z) \tag{4.16}$$

where in the $\overline{\rm MS}$ scheme,

$$\delta Z_{\rm wf} = -\mathcal{N}\frac{\alpha_s}{\pi}\frac{1}{12\epsilon} \quad . \tag{4.17}$$

Finally, there is the Altarelli-Parisi subtraction[18] which factors out the soft singularity and gives a contribution,

$$\sigma_{\rm AP} = \mathcal{N}\left(\frac{m_t^2}{\mu^2}\right)^\epsilon\frac{\alpha_s}{\pi\epsilon}zP_{gg}(z)\sigma_0^\epsilon \tag{4.18}$$

where P_{gg} is the Altarelli-Parisi splitting function,

$$P_{gg}(z) = C_{\rm A}\tilde{P}_{gg}(z) + 2\pi b_0\delta(1-z) \quad . \tag{4.19}$$

The final result, the physical cross section for $gg \to HX$ at next-to-leading order in α_s, is then the sum

$$\hat{\sigma}_{\rm TOT}(gg\to HX) = \sigma_0 + \sigma_{\rm virt} + \sigma_{\rm real} + \sigma_{\rm ch} + \sigma_{\rm wf} + \sigma_{\rm AP} \quad , \tag{4.20}$$

where $\sigma_0 = \sigma_0^\epsilon\big|_{\epsilon=0}$ (with α_s evaluated at μ). It is convenient to write our result as

$$\begin{aligned}\hat{\sigma}_{\rm TOT}(gg\to HX) =&\sigma_0\left\{\delta(1-z) + \frac{\alpha_s(\mu)}{\pi}\left[h(z) + \bar{h}(z)\log\left(\frac{M_{\rm H}^2}{\mu^2}\right)\right.\right.\\ &\left.\left. + \frac{34r}{135}\delta(1-z) - \frac{3r}{20}z(1-z)\right]\right\} + \mathcal{O}(r^2)\end{aligned} \tag{4.21}$$

the functions $h(z)$ and $\bar{h}(z)$ are the same as those of Ref. 2:

$$\begin{aligned}h(z) =&\delta(1-z)\left(\pi^2 + \frac{11}{2}\right) - \frac{11}{2}(1-z)^3\\ &+ 2C_{\rm A}[1+(1-z)^4+z^4]\left[\frac{\log(1-z)}{1-z}\right]_+ - C_{\rm A}z\tilde{P}_{gg}(z)\log z \quad ,\\ \bar{h}(z) =&C_{\rm A}z\tilde{P}_{gg}(z).\end{aligned} \tag{4.22}$$

It is clear that the dominant contributions to the result are just a rescaling of the $r = 0$

result by the ubiquitous factor $1 + 7\tau/60$. Note the cancellation of the $\log(m_t/M_H)$ terms.

(d) $q\bar{q} \to gH$

The process $q\bar{q} \to gH$ proceeds by the diagram of Fig. 3c. The resulting spin and color- averaged cross section is easily found:

$$\sigma(q\bar{q} \to gH) = \frac{\alpha_s^3}{\pi^2 v^2} \frac{(1-z)^3}{486} \left| I\left(\frac{r}{z}, r\right) \right|^2 \quad . \tag{4.23}$$

The integral I, which arises from the triangle diagram of Fig. 1 with one of the gluon legs taken off-shell, has been computed by Bergstrom and Hulth[19] .

$$I(a,b) = 3 \int_0^1 dx \int_0^{1-x} \frac{1-4xy}{1-ax(1-x-y)-bxy} \tag{4.24}$$

If we expand the result in powers of $1/m_t^2$ as we did for the gluon gluon scattering, we find a result which grows with s (as compared to the $gg \to gH$ case which did not have any such terms):

$$\sigma(q\bar{q}) \to gH) \sim \left(1 + \frac{11s + 7M_H^2}{60m_t^2}\right) \quad . \tag{4.25}$$

Since we intend to integrate over parton energies much larger than m_t we must use the exact result of Eq. (4.23) in order to have sensible high energy behavior.

(e) $qg \to qH$

The matrix-element squared for the subprocess $qg \to gH$ can be obtained by crossing from $q\bar{q} \to gH$. The spin and color averaged cross section can then be found by integrating over the n dimensional phase space. Factoring the soft singularity, we find

the physical cross section $\hat{\sigma}$:

$$\hat{\sigma}(qg \to gH) = \frac{\alpha_s(\mu)}{\pi}\left\{ \sigma_0 z P_{gq}(z)\left[\frac{1}{2}\log\left(\frac{s}{\mu^2}\right) + \frac{1}{2} + \log(1-z)\right] + \frac{\sigma_0}{3}(1-z)(3z-7) \right.$$
$$\left. + \frac{2}{3}\sigma_0|_{\tau=0} \int_0^1 d\omega \left(\frac{|I(\tau,r)|^2 - |I(0,r)|^2}{1-\omega} \right) \left[1 + \omega^2 (1-z)^2\right] \right\} \tag{4.26}$$

where $\tau \equiv -s(1-z)(1-\omega)/m_t^2$, and

$$P_{gq} = \frac{4}{3z}\left[1 + (1-z)^2\right] \quad . \tag{4.27}$$

As was the case for the $q\bar{q}$ process, the expansion of this expression in inverse powers of m_t leads to terms which grow with s. Instead, we integrate Eq. (4.26) numerically and give our results in the next section.

5. NUMERICAL RESULTS

In this section we present numerical results for Higgs production in pp collisions at the LHC ($\sqrt{S}$ = 15 TeV) and the SSC ($\sqrt{S}$ = 40 TeV.) We use parton distribution functions from Morfin and Tung[20] : the next-to-leading order set S1 translated into the $\overline{\rm MS}$ prescription and the lowest order set extracted from the same data. Unless otherwise stated we will always use the renormalization scale $\mu = M_{\rm H}$.

Figures 4 and 5 contain the radiatively corrected cross sections for Higgs boson production at the LHC and SSC respectively for m_t equals 150 GeV and 200 GeV. Although these figures include the contribution from gg, qg, $\bar{q}g$, and $q\bar{q}$ initial states the result is completely dominated by the gg initial state. To gauge the effect of the radiative corrections we also plot two versions of the Born result : the first is a consistent leading order result, using α_s, parton distributions and the hard cross section all at leading order, the second is a hybrid result using α_s and parton distributions at next-to-leading order (NLO) convoluted with the hard cross section at Born level. Both

versions are equally correct as they differ at higher order. We see from Figures 4 and 5 that the consistent leading order result is almost 50% larger than the hybrid result. Comparing the NLO result with the two leading order results we see that it is about a factor of 1.5 larger than the consistent leading order result and about a factor of two larger than the hybrid result. The comparison to the hybrid result implies that the $\mathcal{O}(\alpha_s^3)$ contribution is over half of the full NLO result.

To emphasize the significance of the radiative corrections we have plotted the ratio of the radiatively-corrected cross section to the two different Born results in Fig. 6a. This ratio is often called the K factor. Our results are in complete agreement with Ref. 3, where the K-factor is defined using the consistent leading order result, as in the dotted curve in Fig. 6a. From this figure we see that using a next-to-leading order α_s and next-to-leading order parton distributions does not give an improved approximation to the full NLO result but rather it is better to do a consistent leading order calculation. Figure 6b shows the ratio of the qg cross sections to the hybrid Born result. The $q\bar{q}$ contribution is everywhere negligible.

Numerically, the major contribution to the NLO cross section can be obtained by taking the results of the low energy theorem (the $\mathcal{O}(\alpha_s^3)$ result with $r = 0$) and scaling by the factor $(1 + 7r/60)$. To emphasize this we plot in Fig. 7 the ratio of the $\mathcal{O}(\alpha_s^3 r)$ result to the $\mathcal{O}(\alpha_s^3)$ result with $r = 0$ for each subprocess. (These curves all have the 2-loop α_s and the non-leading parton distribution functions.) We see that for the gluon fusion result, the answer is well approximated by the $m_t \to \infty$ results of Ref. 2 and 3. Furthermore, the deviation from the $m_t \to \infty$ result is approximated to better that 1% accuracy by the m_t dependence of the lowest order cross section. For the $q\bar{q}$ and qg subprocesses, the $m_t \to \infty$ limit is a poor approximation over almost the entire kinematic region. This is clearly due to the terms which grow like s/m_t^2 as discussed in Section 4d.

Fig. 8 shows the dependence of the consistent leading order result and the next-to-

leading order result on the renormalization/factorization scale μ for a range of Higgs boson masses. We see that, contrary to naive expectations, the radiative corrections do not generally reduce the dependence of the cross section on μ. One can only expect the next-to-leading order result to have less μ dependence if the radiative corrections are small. Since the radiative corrections are about 100% and, being higher order in α_s, are more scale dependent, the dependence on μ of the NLO result is more severe than the leading order result.

6. CONCLUSIONS

We have computed the $\mathcal{O}(\alpha_s^3 r)$ contributions to $pp \to gH$. They are dominated by the gluon fusion contribution and typically increase the lowest order cross section by a factor of between 1.5 and 2. The lowest order cross section is sensitive to whether the 1-loop or 2-loop α_s is used and which distribution functions are used.

The dominant numerical corrections to the gluon fusion contribution can be found from the $m_t \to \infty$ $\mathcal{O}(\alpha_s^3)$ results of Refs. 2 and 3 by rescaling the cross section by the factor $(1 + 7r/60)$. The smallness of the $\mathcal{O}(\alpha_s^3 r)$ terms demonstrates the valididty of the $m_t \to \infty$ limit for the gluon fusion subprocess. Indeed, Ref. 3 found that the $m_t \to \infty$ results were good to within 15% even for $M_{\rm H} > m_t$.

The determination of the transverse momentum distribution of the Higgs boson requires summing the $\log(M_{\rm H}^2/p_T^2)$ terms which are important at low p_T.[21] The $\mathcal{O}(\alpha_s^3 r)$ terms which we have calculated can be used to extend this summation beyond the leading order.

7. ACKNOWLEDGEMENTS

We are grateful to W. Schaffer and A. Stange for many valuable discussions. We also thank M. Spira for providing us with a copy of his thesis.

APPENDIX A. Symmetrizations

The numerators of the integrals are of the form

$$p \cdot k_1^j \; p \cdot k_2^k \; q \cdot k_1^m \; q \cdot k_2^i \; \times (\text{powers of } p^2,\; q^2,\; \text{and } p \cdot q)$$

where p and q are the loop momenta. Hence all the numerators can be written as contractions of external momenta with products of up to six loop momenta. Since the denominators contain no external momenta, structures such as

$$p^\mu p^\nu p^\rho p^\sigma$$

must be symmetric in all their indices. Therefore, we make the substitution

$$p^\mu p^\nu p^\rho p^\tau \rightarrow C_2 V_4^{\mu\nu\rho\sigma} (p^2)^2$$

where

$$V_4^{\mu\nu\rho\sigma} = g^{\mu\nu} q^{\rho\sigma} + g^{\mu\rho} g^{\nu\sigma} + g^{\mu\sigma} g^{\nu\rho}$$

and

$$C_2 = \frac{1}{n(n+2)}$$

where $n = 4 - 2\epsilon$ is the number of dimensions.

Similar arguments can be made for more complicated combinations. The remaining permutations of four loop momenta are

$$
\begin{aligned}
p^\mu p^\nu p^\rho q^\sigma &\to C_2 V_4^{\mu\nu\rho\sigma} p^2\ p\cdot q, \\
p^\mu p^\nu q^\rho q^\sigma &\to C_{22}\{(n+2)[p^2q^2-(p\cdot q)^2]g^{\mu\nu}g^{\rho\sigma} \\
&\quad + (n\,(p\cdot q)^2 - p^2q^2)V_4^{\mu\nu\rho\sigma}\},
\end{aligned}
$$

For products of six loop momenta we define

$$
V_6^{\mu\nu\rho\alpha\beta\gamma} = g^{\mu\nu}V_4^{\rho\alpha\beta\gamma} + g^{\mu\rho}V_4^{\nu\alpha\beta\gamma} + g^{\mu\alpha}V_4^{\nu\rho\beta\gamma} + g^{\mu\beta}V_4^{\nu\rho\alpha\gamma} + g^{\mu\gamma}V_4^{\nu\rho\alpha\beta}
$$

The symmetrizations of six loop momenta are

$$
\begin{aligned}
p^\mu p^\nu p^\rho p^\alpha p^\beta p^\gamma &\to C_3 V_6^{\mu\nu\rho\alpha\beta\gamma}(p^2)^3 \quad , \\
p^\mu p^\nu p^\rho p^\alpha p^\beta q^\gamma &\to C_3 V_6^{\mu\nu\rho\alpha\beta\gamma}(p^2)^2 p\cdot q \quad , \\
p^\mu p^\nu p^\rho p^\sigma q^\alpha q^\beta &\to C_{24}p^2\{(n+4)\left[p^2q^2-(p\cdot q)^2\right]g^{\alpha\beta}V_4^{\mu\nu\rho\sigma} \\
&\quad + [n\,(p\cdot q)^2 - p^2q^2]V_6^{\mu\nu\rho\sigma\alpha\beta}\} \quad , \\
p^\mu p^\nu p^\rho q^\alpha q^\beta q^\gamma &\to C_{24}\{(n+4)\left[p^2q^2p\cdot q-(p\cdot q)^3\right](g^{\alpha\beta}V_4^{\gamma\mu\nu\rho} + g^{\alpha\gamma}V_4^{\beta\mu\nu\rho} \\
&\quad + g^{\beta\gamma}V_4^{\alpha\mu\nu\rho}) + [(n+2)(p\cdot q)^3 - 3p^2q^2p\cdot q]V_6^{\mu\nu\rho\alpha\beta\gamma}\} \quad .
\end{aligned}
$$

The various coefficients are

$$
\begin{aligned}
C_{22} &= \frac{1}{n(n-1)(n+2)} \quad , \\
C_3 &= \frac{1}{n(n+2)(n+4)} \quad , \\
C_{24} &= \frac{1}{n(n-1)(n+2)(n+4)} \quad .
\end{aligned}
$$

APPENDIX B. Integrals

In this appendix we present the results necessary to obtain the 2-loop integrals used in this paper. We use dimensional regularization with $n = 4 - 2\epsilon$. The integrals form two basic classes: the first where all denominators are massive (arising from diagrams VII and VIII) and the second where there are massless denominators (arising from diagrams I-VI).

The first class of integrals has the general form:

$$B_{jkl} \equiv -2(4\pi)^4 \int \frac{d^n p}{(2\pi)^n} \int \frac{d^n q}{(2\pi)^n} \frac{1}{[(p+q)^2 - m^2]^j (p^2 - M^2)^k (q^2 - M^2)^l} \quad . \tag{B1}$$

We will need B_{jkl} with $j = 1, 2, 3$ and $j + k + l < 10$. Using integration by parts on the B_{1kl} leads to the following recursion relation[22,12]

$$B_{1,j+1,l} = \frac{1}{2jM^2} \left[\left(n - 1 - 2j - m^2 \frac{\partial}{\partial m^2} \right) B_{1,j,l} + \frac{\partial}{\partial m^2} B_{1,j,l-1} - \frac{\partial}{\partial m^2} B_{1,j-1,l} \right]. \tag{B2}$$

The B_{2kl} and B_{3kl} can be obtained from the B_{1kl} by differentiation:

$$B_{j+1,k,l} = \frac{1}{j} \frac{\partial}{\partial m^2} B_{j,k,l} \quad .$$

Hence we need only calculate B_{111}. This integral has been given in a power series in $b \equiv m^2/M^2$ in Ref. 12. However, we need to carry the expansion in b further than in this reference. We find:

$$\begin{aligned} B_{111} =& M^2 \left\{ \frac{b+2}{\epsilon^2} + \frac{1}{\epsilon} \left(6 + 3b - 2b \log b \right) - b \left(2 + \frac{b}{3} + \frac{b^2}{30} + \frac{b^3}{210} \right) \log b + b \log^2 b \right. \\ & \left. + 14 + b \left(-1 + \frac{8}{9} b + \frac{31}{450} b^2 + \frac{389}{44100} b^3 \right) \right\} \quad . \end{aligned} \tag{B3}$$

For most of the diagrams any infinities come from the loop momentum integrals and so there is no need to keep terms which vanish as $n \to 4$ in the integrals. The exception

is diagram VIII which has infrared divergences arising in the Feynman integrals. These divergences come from terms of $\mathcal{O}(1/m^2)$ arising in the B_{3jk} integrals. Thus, the terms of $\mathcal{O}(1/m^2)$ in the B_{3jk} need to be calculated to $\mathcal{O}(\epsilon^2)$. Rather than rederive the entire series of integrals keeping terms to $\mathcal{O}(\epsilon^2)$ we notice that the $\mathcal{O}(1/m^2)$ terms come from a particular part of the integral in Eq. (B1), that in which $p = -q$. Therefore, changing variables to $p \to p - q$ and dropping p except in the denominator m^2 we find

$$B_{3kl} \to -2(4\pi)^4 \int \frac{d^n p}{(2\pi)^n} \frac{1}{(p^2 - m^2)^3} \int \frac{d^n q}{(2\pi)^n} \frac{1}{(q^2 - M^2)^{k+l}} \quad , \tag{B4}$$

where we have kept only the terms of $\mathcal{O}(1/m^2)$. Eq. (B4) can also be verified by brute force calculation.

The integrals which contain massless denominators are B_{jkl} with one of the masses taken to zero

$$\tilde{B}_{jkl} = B_{jkl}\Big|_{m=0} . \tag{B5}$$

We will need the result for $j = 1, 2$. For the case of the $\tilde{B}_{1jk}$ one may simply take the limit $m \to 0$ in the expressions for B_{1jk} since the limit is well defined. However, the $\tilde{B}_{2kl}$ have infrared divergences and cannot be derived directly from the B_{2kl}. Instead, using integration by parts we derive another recursion relation

$$\tilde{B}_{2kl} = \tilde{B}_{2,k+1,l-1} + (n - 2k - 3)\tilde{B}_{1,k+1,l} - 2(k+1)M^2 \tilde{B}_{1,k+2,l} \quad . \tag{B6}$$

Since $\tilde{B}_{2k0} = 0$, the $\tilde{B}_{2k1}$ depend only on the $\tilde{B}_{1kl}$ and the rest of the integrals follow. Alternatively, one may use the explicit formula of Ref. 23:

$$\begin{aligned} \tilde{B}_{jkl} = & \frac{1}{2}(-1)^{j+k+l} \left(\frac{4\pi}{M^2}\right)^{2\epsilon} (M^2)^{4-j-k-l} \\ & \times \frac{\Gamma(k+l+j-n)\Gamma(k+j-n/2)\Gamma(l+j-n/2)\Gamma(n/2-j)}{\Gamma(k+l+2j-n)\Gamma(k)\Gamma(l)\Gamma(n/2)} \quad . \end{aligned} \tag{B7}$$

We have checked that the two approaches give identical results.

APPENDIX C. Virtual Diagrams for $gg \to H$

The results of the various diagrams can be separated into two-gauge invariant sets: contributions proportional to the group factors C_F and C_A. The C_F terms are proportional to the diagrams for $H \to \gamma\gamma$ computed in Ref 11. We present them here for completeness, written in the form of Eq. (3.1).

$$\mathcal{A}_i^{\mu\nu} = -\mathcal{N}^2 \frac{\alpha_s^2}{2\pi^2 v} \left(a_i g^{\mu\nu} k_1 \cdot k_2 + b_i k_1^\nu k_2^\mu\right) \quad .$$

In this appendix we present only the real part of each amplitude. Only diagrams VII and VIII have imaginary parts: these are given in Appendix D. Our results for the diagrams contributing to $H \to \gamma\gamma$ are :

$$\begin{aligned}
a_{\rm I} &= \left(\frac{C_F}{16}\right)\frac{1}{45}\left[\frac{135}{r}\left(-\frac{2}{\epsilon^2}+\frac{1}{\epsilon}+\frac{37}{18}\right)-\frac{177}{\epsilon}+7-\frac{r}{14}\left(\frac{277}{\epsilon}+\frac{12821}{30}\right)\right] \quad , \\
b_{\rm I} &= \left(\frac{C_F}{16}\right)\frac{1}{45}\left[\frac{123}{\epsilon}+47+\frac{r}{7}\left(\frac{223}{2\epsilon}+\frac{2924}{15}\right)\right] \quad , \\
a_{\rm II} &= \left(\frac{C_F}{16}\right)\frac{1}{45}\left[\frac{270}{r}\left(\frac{2}{\epsilon^2}-\frac{1}{\epsilon}-\frac{1}{18}\right)-\frac{6}{\epsilon}-\frac{872}{3}-\frac{r}{7}\left(\frac{17}{\epsilon}+\frac{6719}{60}\right)\right] \quad , \\
b_{\rm II} &= \left(\frac{C_F}{16}\right)\frac{1}{45}\left[\frac{114}{\epsilon}+\frac{388}{3}+\frac{r}{7}\left(\frac{71}{\epsilon}+\frac{566}{5}\right)\right] \quad , \\
a_{\rm III} &= \left(\frac{2C_F-C_A}{32}\right)\frac{1}{3}\left[-\frac{36}{r}+\frac{4d_r}{\epsilon}+\frac{34}{9}+\frac{1151r}{2700}\right] \quad , \\
b_{\rm III} &= \left(\frac{2C_F-C_A}{32}\right)\frac{1}{3}\left[-\frac{4d_r}{\epsilon}-\frac{2}{9}-\frac{109r}{1350}\right] \quad , \\
a_{\rm IV} &= \left(\frac{C_F}{16}\right)\frac{1}{3}\left[\frac{36}{r}+\frac{16d_r}{\epsilon}-\frac{226}{9}+\frac{6287r}{2700}\right] \quad , \\
b_{\rm IV} &= \left(\frac{C_F}{16}\right)\frac{1}{3}\left[-\frac{16d_r}{\epsilon}+\frac{194}{9}-\frac{361r}{135}\right] \quad ,
\end{aligned} \tag{C1}$$

where

$$d_r \equiv 1 + \frac{7r}{120} \quad . \tag{C2}$$

The remaining, purely non-abelian, diagrams are

$$
\begin{aligned}
a_{\rm V} &= \left(\frac{C_{\rm A}}{12}\right)\left[-\frac{1}{r}\left(\frac{9}{4\epsilon}+\frac{15}{8}\right)+\frac{3}{\epsilon}-\frac{85}{72}+\frac{r}{180}\left(\frac{29}{\epsilon}+\frac{2497}{48}\right)\right] \quad , \\
b_{\rm V} &= \left(\frac{C_{\rm A}}{12}\right)\left[-\frac{3}{r}+\frac{10}{9}-\frac{r}{180}\left(\frac{29}{\epsilon}+\frac{6181}{120}\right)\right] \quad , \\
a_{\rm VI} &= \left(\frac{C_{\rm A}}{12}\right)\left[-\frac{1}{r}\left(\frac{9}{2\epsilon}+\frac{15}{4}\right)+\frac{113}{36}+\frac{r}{8}\left(-\frac{1}{\epsilon}+\frac{517}{2700}\right)\right] \quad , \\
b_{\rm VI} &= \left(\frac{C_{\rm A}}{12}\right)\left[-\frac{59}{18}+\frac{r}{8}\left(\frac{1}{\epsilon}-\frac{197}{1350}\right)\right] \quad , \\
a_{\rm VII} &= \left(\frac{C_{\rm A}}{12}\right)\left[\frac{9}{r}\left(-\frac{3}{\epsilon}+\frac{11}{2}\right)+\frac{1}{3}\left(13+\frac{43r}{60}\right)\log r-\frac{164}{9}-\frac{73r}{120}\right] \quad , \\
b_{\rm VII} &= \left(\frac{C_{\rm A}}{12}\right)\left[\frac{1}{3}\left(1+\frac{r}{15}\right)\log r-\frac{19}{18}-\frac{r}{30}\right] \quad , \\
a_{\rm VIII} &= \left(\frac{C_{\rm A}}{12}\right)\frac{1}{6}\left[\frac{135}{r}\left(\frac{1}{\epsilon}-\frac{7}{6}\right)+\left(-\frac{12r^{-\epsilon}}{\epsilon^2}+8\pi^2\right)d_r-\left(13+\frac{r}{60}\right)\log r\right. \\
&\quad \left.-\frac{30}{\epsilon}+\frac{257}{3}-\frac{r}{20}\left(\frac{92}{3\epsilon}+\frac{239}{18}\right)\right] \quad , \\
b_{\rm VIII} &= \left(\frac{C_{\rm A}}{12}\right)\frac{1}{6}\left[\left(\frac{12r^{-\epsilon}}{\epsilon^2}-8\pi^2\right)d_r-\left(1+\frac{23r}{30}\right)\log r\right. \\
&\quad \left.+\frac{30}{\epsilon}-\frac{125}{6}+\frac{r}{15}\left(\frac{23}{\epsilon}+\frac{547}{12}\right)\right] \quad .
\end{aligned}
\tag{C3}
$$

We also include in our definition of the virtual diagrams the mass counterterms:

$$
a_{\rm mass} = -b_{\rm mass} = C_{\rm F}\left[1+\frac{7}{120}\frac{r}{\epsilon}+\frac{7r}{36}\right] \tag{C4}
$$

Multiplying by the appropriate number of each type of diagram, we find our result,

$$
\begin{aligned}
a_{\rm TOT} =& 4a_{\rm I}+2a_{\rm II}+4a_{\rm III}+2a_{\rm IV}+4a_{\rm V}+2a_{\rm VI}+a_{\rm VII}+2a_{\rm VIII}+a_{\rm mass} \\
=& C_{\rm A}\left[\left(-\frac{r^{-\epsilon}}{3\epsilon^2}+\frac{2\pi^2}{9}\right)\left[1+\frac{7r}{120}(1+\epsilon)\right]+\frac{5}{6}+\frac{29r}{2160}\right]-\frac{C_{\rm F}}{2}\left[1-\frac{61r}{270}\right] \\
=& -b_{\rm TOT} \quad .
\end{aligned}
$$

Combining with the Born amplitude of Eq. (2.4), this give the result of Eq. (4.4) to $\mathcal{O}(r^2)$. Note that there are only two topologically distict diagrams of type VI, whereas there are four of type V; this is because reversing the quark line in diagram VI is equivalent to exchanging the two virtual gluons. The terms of $\mathcal{O}(1/r)$ vanish in the sum, as required by gauge invariance.

APPENDIX D. Checks on Virtual Diagrams

There are several checks which can be performed on the diagrams shown in Figure 2, VII and VIII. Both the coefficients of the logarithms and the finite terms can be simply obtained. We begin by noting that these diagrams can be written in terms of the triangle diagram of Fig. 1 with both gluons off-shell. Then, for example, diagram VII can be written as,

$$\begin{aligned}\mathcal{A}_{\rm VII}^{\mu\nu} =& 4\pi\alpha_s f_{\rm ACE} f_{\rm BDE}(2g_{\mu\nu}g_{\lambda\sigma} - g_{\mu\sigma}g_{\nu\lambda} - g_{\mu\lambda}g_{\nu\sigma}) \\ &\times \int \frac{d^n q}{(2\pi)^n}\frac{1}{q^2}\frac{1}{(k_1+k_2-q)^2} i\Gamma_{\rm CD}^{\sigma\lambda}(q, k_1+k_2-q)\end{aligned} \tag{D1}$$

where $\Gamma_{\rm CD}^{\sigma\lambda}(q, k_1+k_2-q)$ is the triangle diagram of Fig. 1 with both gluons evaluated off-shell.

The coefficients of the logarithms can be obtained by using the Cutkosky cutting rules to find the imaginary parts of the amplitudes, which amounts to replacing the massless gluon propagators by $-2\pi i\delta(q^2)$ and $-2\pi i\delta((q-k_1-k_2)^2)$ and adding an overall factor of $1/2$. The ggH 3-point function is then given by:

$$\delta(q_1^2)\delta(q_2^2)\Gamma_{\rm CD}^{\sigma\lambda}(q_1, q_2) = -\frac{\alpha_s}{2\pi v}\delta_{\rm CD}\mathcal{N}\left\{\frac{1}{3}(1+\frac{7\tau}{120})\left(\frac{M_{\rm H}^2}{2}g^{\sigma\lambda} - q_2^\sigma q_1^\lambda\right) - \frac{\tau}{360}q_2^\lambda q_1^\sigma\right\} \tag{D2}$$

Substituting Eq. (D2) into Eq. (D1) and evaluating the $d^n q$ integral explicitly, we find

$$Im(\mathcal{A}_{\rm VII}^{\mu\nu}) = \frac{\alpha_s^2}{8\pi v}\delta_{\rm AB}\mathcal{N}^2\left(\frac{C_{\rm A}}{3}\right)\left[\frac{M_{\rm H}^2}{6}g^{\mu\nu}\left(13+\frac{43\tau}{60}\right) + \frac{1}{3}k_1^\nu k_2^\mu\left(1+\frac{\tau}{15}\right)\right] \quad . \tag{D3}$$

The imaginary part of the box diagram, Figure 2, VIII can be found in an identical

manner:

$$Im(\mathcal{A}^{\mu\nu}_{\rm VIII}) = \frac{\alpha_s^2}{16\pi v}\delta_{AB}N^2\left(\frac{C_A}{3}\right)\left\{M_H^2 g^{\mu\nu}\left[\left(\frac{2}{\epsilon} - \log r - \frac{13}{6}\right)\right.\right.$$
$$\left. + \frac{r}{60}\left(\frac{7}{\epsilon} - \frac{1}{60} - \frac{7}{2}\log r\right)\right]$$
$$\left. + k_1^\nu k_2^\mu\left[\left(-\frac{4}{\epsilon} + 2\log r - \frac{1}{3}\right) + \frac{r}{30}\left(-\frac{7}{\epsilon} + \frac{7}{2}\log r - \frac{23}{3}\right)\right]\right\} \tag{D4}$$

The logarithms are then obtained by noting that they always enter as $\log(-r) = i\pi + \log r$.

In order to extract the $\frac{1}{\epsilon}$ singularities in diagram VII, we note that they arise from the region where $q^2 = 0$ and hence may be obtained by setting $q^2 = 0$ in the numerator of Eq. (D1). In this region Γ is easily evaluated analytically. The remaining momentum integral over q is straightforwardly performed and the correct $1/\epsilon$ terms obtained. The singularities from diagram VIII can be found in an identical manner.

REFERENCES

1. For a review of Higgs boson phenomenology, see J. Gunion *et. al.*, *The Higgs Hunter's Guide* (Addison-Wesley, Menlo Park, 1991); M. Chanowitz, *Ann. Rev. Nucl. Part. Phys.* **38** (1988) 323.

2. S. Dawson, *Nucl. Phys.* **B359** (1991) 283; A. Djouadi, M. Spira and P. Zerwas, *Phys. Lett.* **B264** (1991)441.

3. D. Graudenz, M. Spira, P. Zerwas, *Phys. Rev. Lett.* **70** (1993) 1372; M. Spira, Ph.D Thesis, Aachen, 1993.

4. P. Langacker, M. Luo, and A. Mann, *Rev. Mod. Phys.* **64** (1992) 87 .

5. T. Mori, *Proc. of the XXVI International Conference on High Energy Physics*, Dallas, Texas, (1992)1321.

6. F. Wilczek, *Phys. Rev. Lett.* **39** (1977) 1304; J. Ellis, M. Gaillard, D. Nanopoulos, and C. Sachrajda, *Phys. Lett.* **83B** (1979) 339; H. Georgi, S. Glashow, M. Machacek, and D. Nanopoulos, *Phys. Rev. Lett.* **40** (1978) 692; T. Rizzo, *Phys. Rev.* **D22** (1980) 178.

7. A. Vainshtein, M. Voloshin, V. Zakharov, and M. Shifman, *Sov. J. Nucl. Phys.* **30** (1979) 711; A. Vainshtein, V. Zakharov, and M. Shifman, *Sov. Phys. Usp.* **23** (1980) 429; M. Voloshin, *Sov. J. Nucl. Phys.* **44** (1986) 478.

8. E. Braaten and J. Leveille, *Phys. Rev.* **D22** (1980) 715; M. Drees and K. Hikasa, *Phys. Lett.* **B240** (1990) 455.

9. S. Adler and W. Bardeen, *Phys. Rev.* **D4** (1971) 3045.

10. R. Kauffman and W. Schaffer, BNL-49061, 1993, to be published in *Phys. Rev.* **D**; A. Djouadi, M. Spira, and P. Zerwas, *Phys. Lett.* **B311** (1993) 255.

11. S. Dawson and R. Kauffman, *Phys. Rev.* **D47** (1993), 1264.

12. F. Hoogeveen, *Nucl. Phys.* **B259** (1985) 19.

13. J. van der Bij and M. Veltman, *Nucl. Phys.* **B231** (1984) 205.

14. G. Passarino and M. Veltman, *Nucl. Phys.* **B160** (1979) 151.

15. H. Zheng and D. Wu, *Phys. Rev.* **D42** (1990) 3760; A. Djouadi, M. Spira, J. van der Bij, and P.Zerwas, *Phys. Lett.* **B257** (1991) 187; K. Melnikov and O. Yakovlev, *Phys. Lett.* **B312** (1993) 179; A. Djouadi, M. Spira, and P. Zerwas, *Phys. Lett.* **B311** (1993) 255.

16. R.Ellis, I. Hinchliffe, M. Soldate and J. Van der Bij, *Nucl. Phys.* **B297** (1988) 221.

17. J. Collins, F. Wilczek, *Phys. Rev.* **D18** (1978) 242; W. Marciano, *Phys. Rev.* **D29** (1984) 580.

18. G. Altarelli and G. Parisi, *Nucl. Phys.* **B126** (1977) 298.

19. L.Bergstrom and G. Hulth, *Nucl. Phys.* **B259** (1985) 137.

20. J. Morfin and W. Tung, *Z. Phys.* *C* **52** (1991) 13.

21. R. P. Kauffman, *Phys. Rev.* **D44** (1991) 1415; *ibid* **D45** (1992) 1512; I. Hinchliffe and S. Novaes. *Phys. Rev.* **D38** (1988) 3475; C.-P. Yuan, *Phys. Lett.* **B283** (1992) 395.

22. G. t'Hooft and M. Veltman, *Nucl. Phys.* **B44** (1972) 189.

23. A. Denner, W. Hollik, and B. Lampe, CERN-TH.6874/93, April 1993; R. Scharf, Diploma Thesis, Wurzburg, 1991.

FIGURE CAPTIONS

1. Top quark loop contributing to $gg \to H$.

2. Two-loop diagrams contributing to $gg \to H$.

3. Real diagrams contributing to $gg \to gH$ and to $q\bar{q} \to gH$.

4. Lowest order (dotted and dashed) and radiatively corrected (solid) cross section for $pp \to HX$ at the LHC, $\sqrt{S} = 15$ TeV. The curves labelled LO pdf and NLO pdf use the lowest order and next to leading order parton distribution functions of Morfin and Tung, respectively.

5. Lowest order (dotted and dashed) and radiatively corrected (solid) cross section for $pp \to HX$ at the SSC, $\sqrt{S} = 40$ TeV.

6. a: Ratio of the radiatively corrected cross section (Eq. (4.21)) to the Born cross section of Eq. (2.5) at the LHC, $\sqrt{S} = 15$ TeV and the SSC, $\sqrt{S} = 40$ TeV, with $m_t = 200$ GeV. b: Ratio of the qg and $\bar{q}g$ cross sections to the Born cross section (with NLO pdfs and 2 loop α_s) of Eq. (2.5) at the LHC, $\sqrt{S} = 15$ TeV and the SSC,$\sqrt{S} = 40$ TeV, with $m_t = 200$ GeV.

7. Ratio of the $\mathcal{O}(\alpha_s^3 r)$ radiatively corrected cross sections to the $\mathcal{O}(\alpha_s^3)$ results with $r = 0$ (labelled $\sigma(m_t \to \infty)$ for each subprocess.

8. Lowest order with LO pdfs and 1 loop α_s (dotted) and radiatively corrected (solid) cross section as a function of μ for $M_{\rm H} = 50$, 100, 200 and 500 GeV at the SSC, $\sqrt{S} = 40$ TeV.

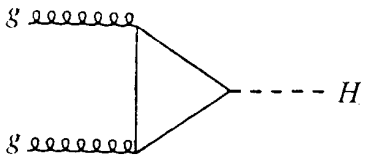

Figure 1

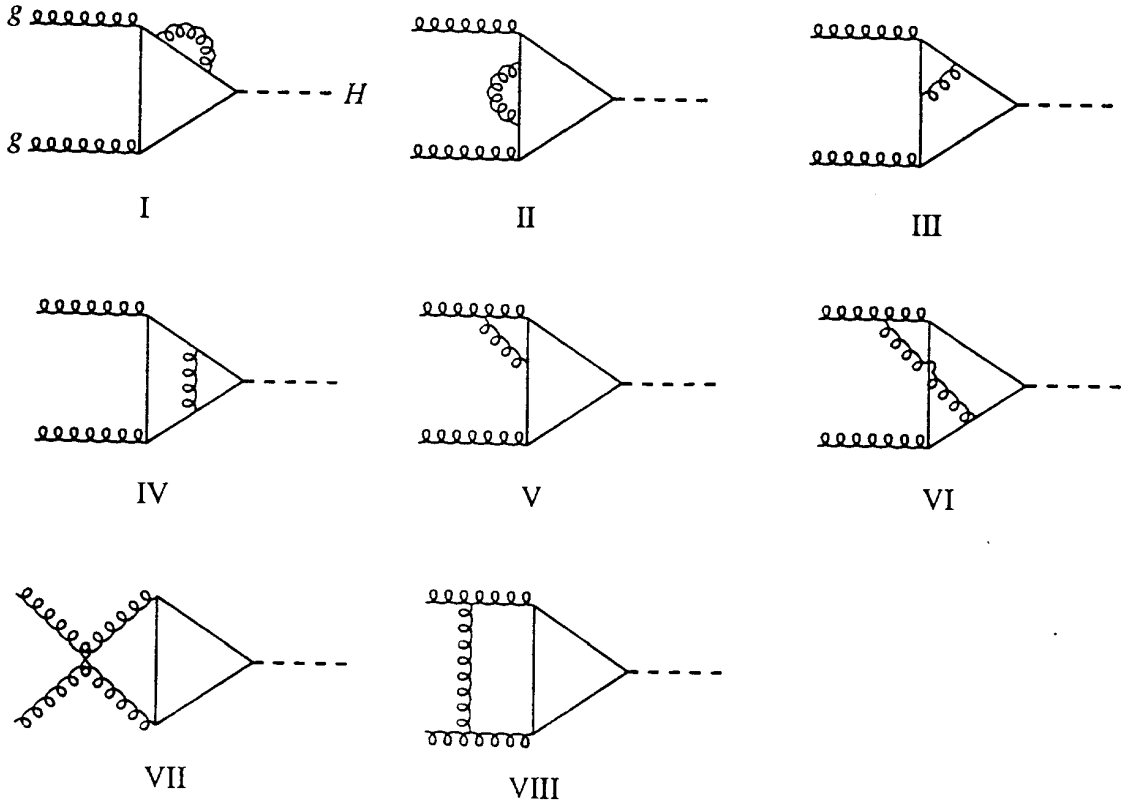

Figure 2

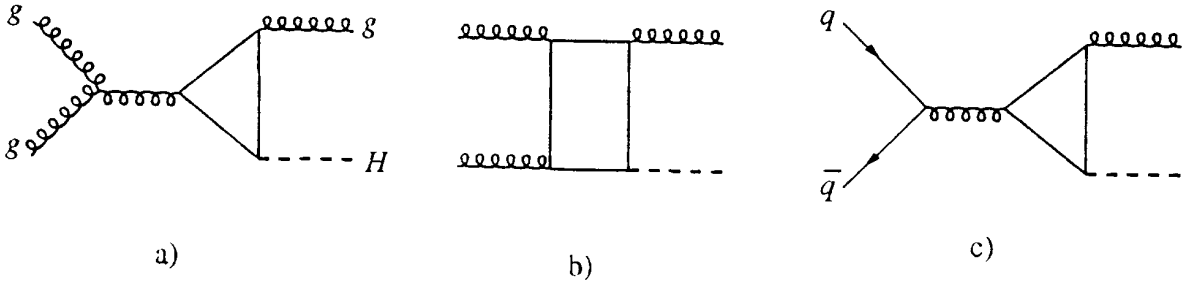

Figure 3

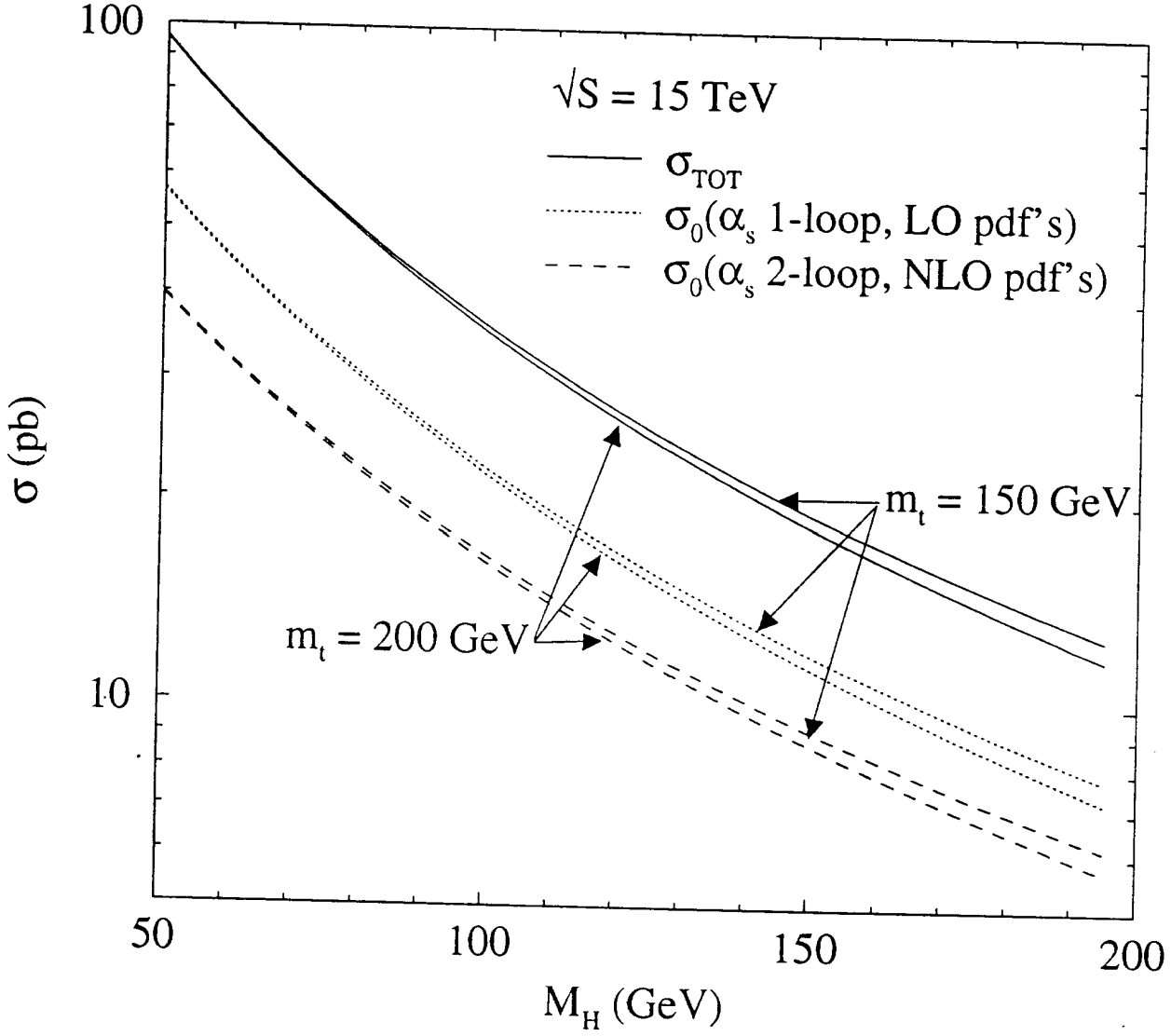
100
10
σ (pb)
√S = 15 TeV
σ_TOT
σ_0(α_s 1-loop, LO pdf's)
σ_0(α_s 2-loop, NLO pdf's)
m_t = 150 GeV
m_t = 200 GeV
50
100
150
200
M_H (GeV)

Figure 4

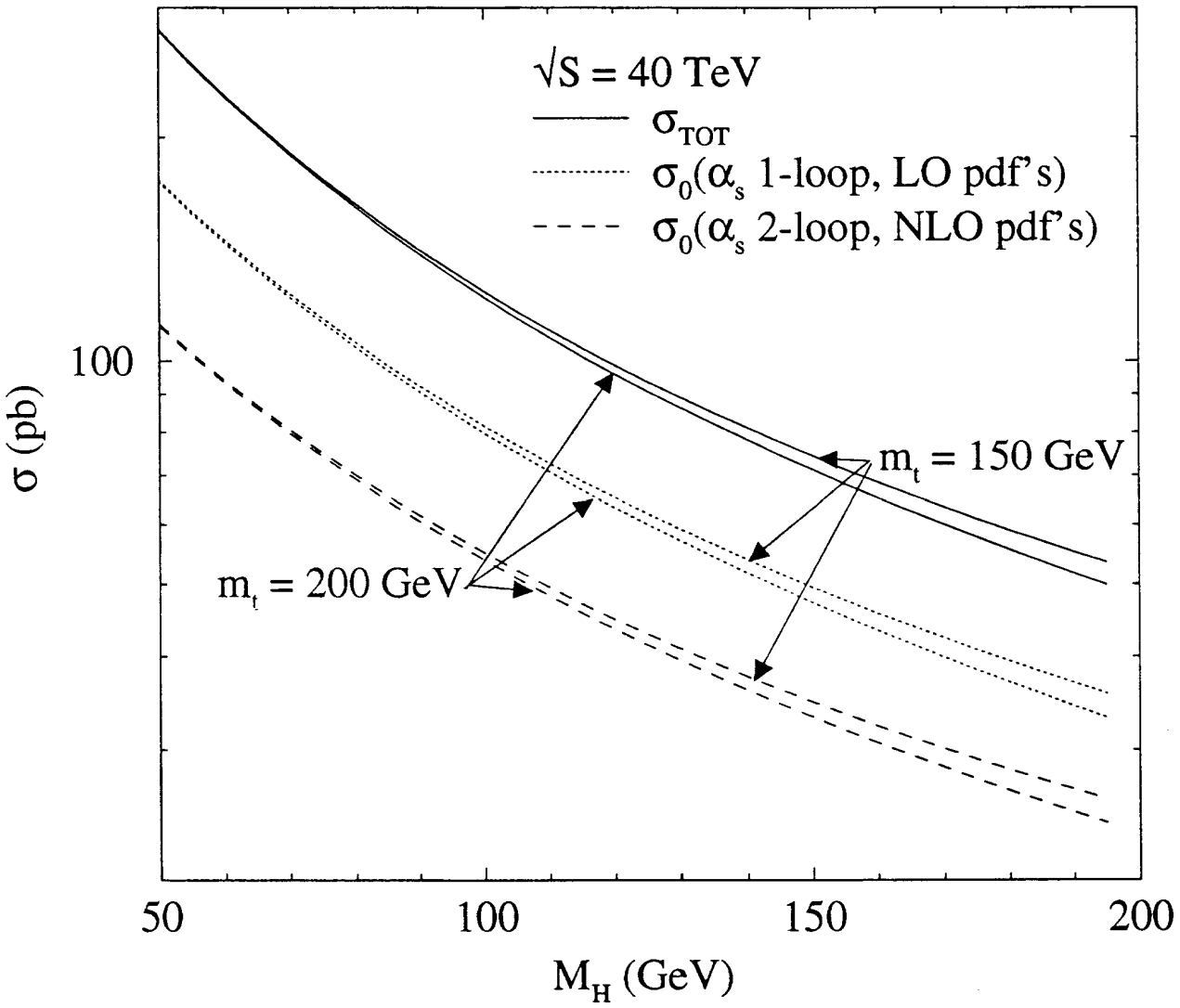
√S = 40 TeV
σ_TOT
σ_0(α_s 1-loop, LO pdf's)
σ_0(α_s 2-loop, NLO pdf's)
m_t = 150 GeV
m_t = 200 GeV
σ (pb)
100
50
100
150
200
M_H (GeV)

Figure 5

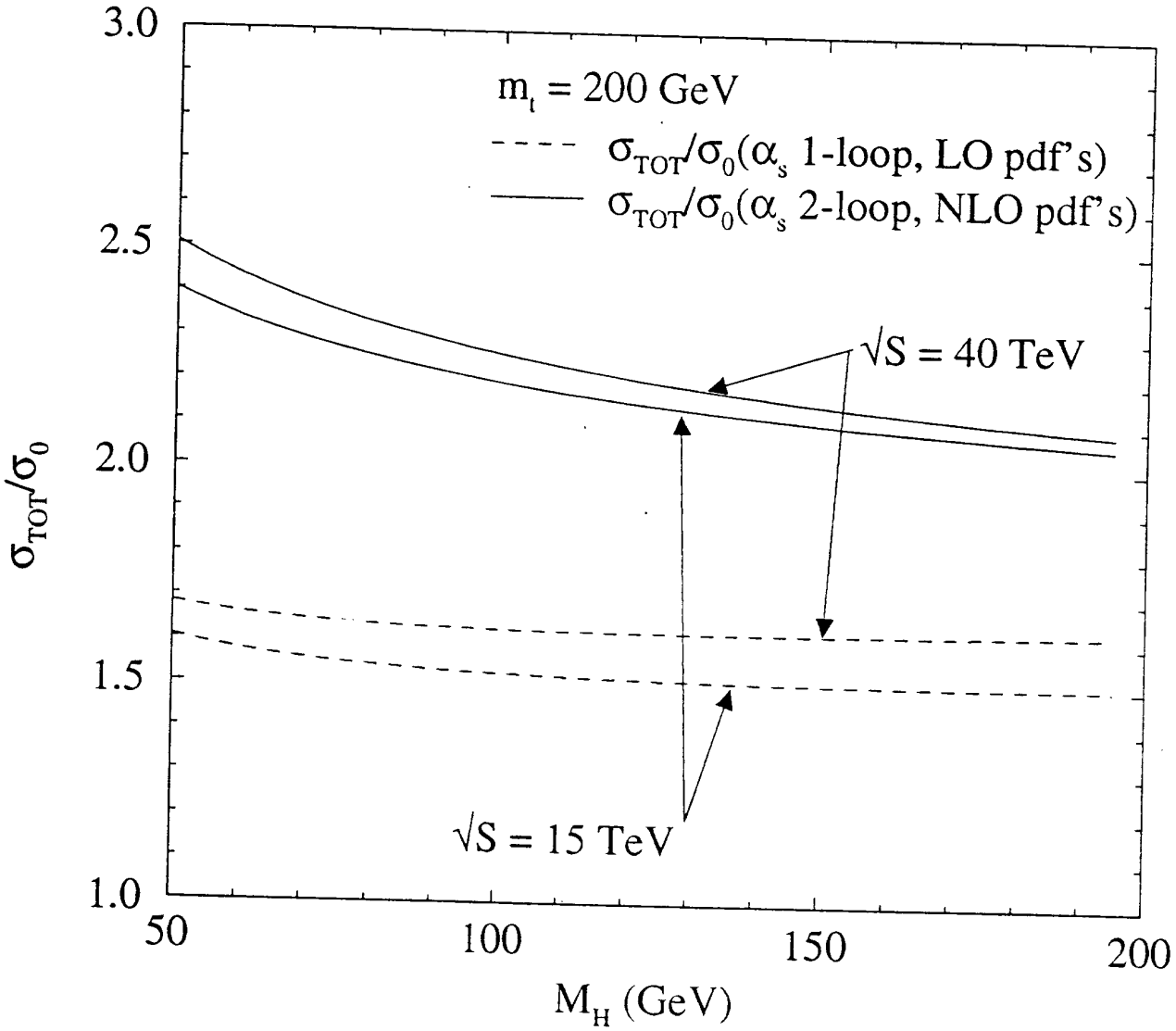
3.0
2.5
2.0
1.5
1.0
50
100
150
200
m_t = 200 GeV
$\sigma_{TOT}/\sigma_0(\alpha_s$ 1-loop, LO pdf's)
$\sigma_{TOT}/\sigma_0(\alpha_s$ 2-loop, NLO pdf's)
√S = 40 TeV
√S = 15 TeV
σ_{TOT}/σ_0
M_H (GeV)

Figure 6a

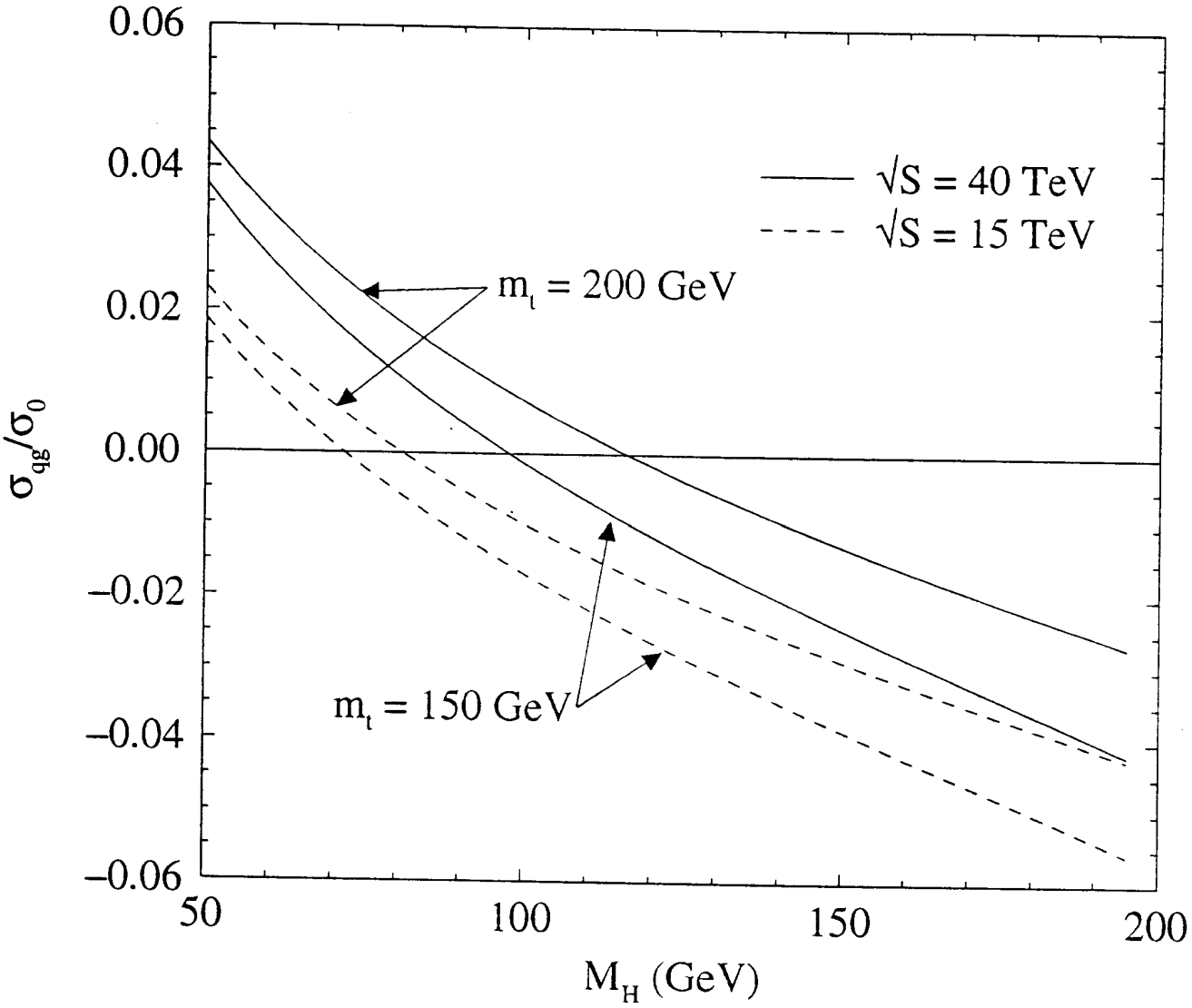
0.06
0.04
0.02
0.00
–0.02
–0.04
–0.06
50
100
150
200
σ_{qg}/σ_0
M_H (GeV)
$\sqrt{S}$ = 40 TeV
$\sqrt{S}$ = 15 TeV
m_t = 200 GeV
m_t = 150 GeV

Figure 6b

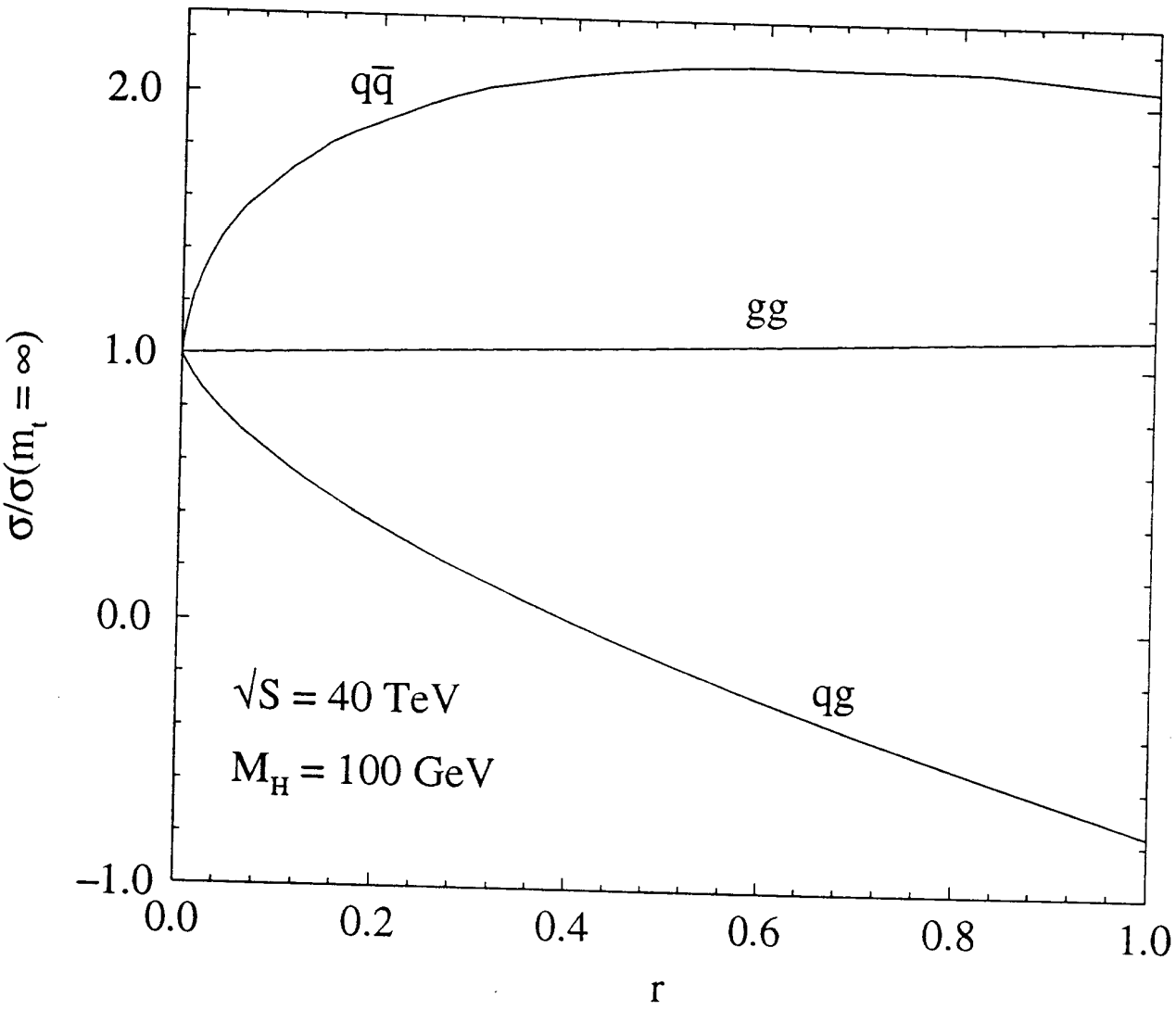

Figure 7

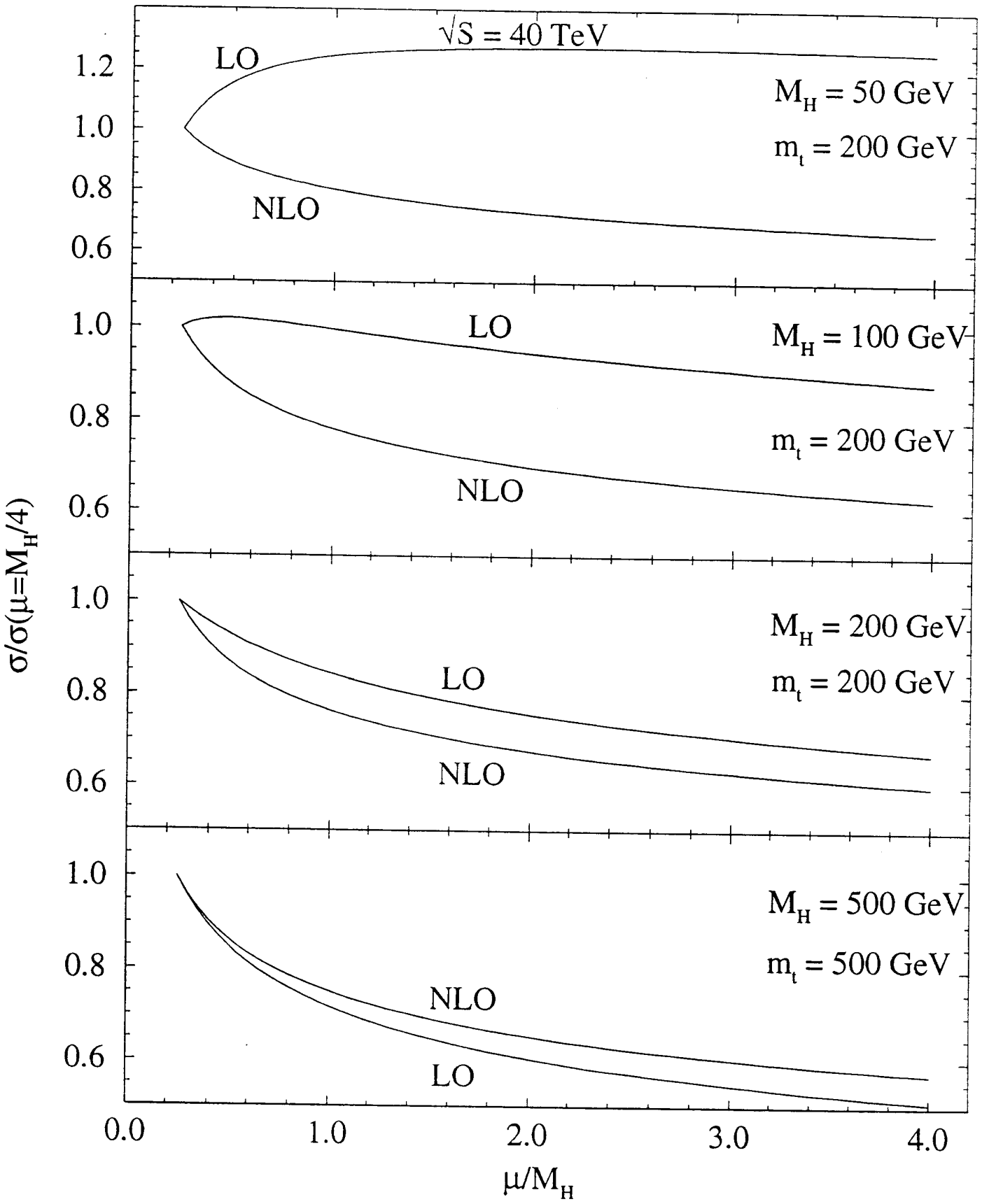
√S = 40 TeV
LO
NLO
M_H = 50 GeV
m_t = 200 GeV
M_H = 100 GeV
m_t = 200 GeV
M_H = 200 GeV
m_t = 200 GeV
M_H = 500 GeV
m_t = 500 GeV
σ/σ(μ=M_H/4)
μ/M_H
1.2
1.0
0.8
0.6
0.0
1.0
2.0
3.0
4.0

Figure 8